

Nonlinear mechanics of a ring structure subjected to multi-pairs of evenly distributed equal radial forces

Q. Chen¹ · F. Sun² · Z. Y. Li^{1,3} · L. Taxis⁴ · N. Pugno^{4,5,6}

Received: 8 December 2016 / Revised: 15 February 2017 / Accepted: 9 March 2017 / Published online: 8 May 2017

© The Chinese Society of Theoretical and Applied Mechanics; Institute of Mechanics, Chinese Academy of Sciences and Springer-Verlag Berlin Heidelberg 2017

Abstract Combining the elastica theory, finite element (FE) analysis, and a geometrical topological experiment, we studied the mechanical behavior of a ring subjected to multi-pairs of evenly distributed equal radial forces by looking at its seven distinct states. The results showed that the theoretical predictions of the ring deformation and strain energy matched the FE results very well, and that the ring deformations were comparable to the topological experiment. Moreover, no matter whether the ring was compressed or tensioned by N -pairs of forces, the ring always tended to be regular polygons with $2N$ sides as the force increased, and a proper compressive force deformed the ring into exquisite flower-like patterns. The present study solves a basic mechanical problem of a ring

subjected to lateral forces, which can be useful for studying the relevant mechanical behavior of ring structures from the nano- to the macro-scale.

Keywords Ring structures · Mechanical properties · Shape · Strain energy

Electronic supplementary material The online version of this article (doi:10.1007/s10409-017-0665-8) contains supplementary material, which is available to authorized users.

✉ Q. Chen
chenq999@gmail.com

¹ Biomechanics Laboratory, School of Biological Science and Medical Engineering, Southeast University, Nanjing 210096, China

² State Key Laboratory of Mechanics and Control of Mechanical Structures, Nanjing University of Aeronautics and Astronautics, Nanjing 210096, China

³ School of Chemistry, Physics and Mechanical Engineering, Queensland University of Technology (QUT), Brisbane, QLD 4001, Australia

⁴ Laboratory of Bio-Inspired and Graphene Nanomechanics, Department of Civil, Environmental and Mechanical Engineering, University of Trento, 38123 Trento, Italy

⁵ School of Engineering and Materials Science, Queen Mary University of London, Mile End Road, London E1 4NS, UK

⁶ Ket Lab, Italian Space Agency, Via del Politecnico snc, 00133 Rome, Italy

1 Introduction

Ring structures are very common from the nano-scale up to the macro-scale. Such structures include two-dimensional (2D) rings formed from bars, e.g., 2D carbon-nanorings [1], and three-dimensional (3D) rings (or cylindrical tubes) formed from thin plates, e.g., 3D steel/aluminum tubes [2]. They generally exhibit variable geometries under different lateral loading conditions, and their mechanical behaviors under conditions such as buckling [1], collapse [2], and impact dynamics [3] have been studied. Carbon nanorings, for example, become elliptical before the buckling of the carbon nanotube [1], and cross-sections of metallic tubes deformed inelastically become double-symmetric [2,3] with plastic hinges. Thus, understanding mechanics of ring structures under lateral loads is beneficial to the present scientific community.

Two-dimensional rings subjected to lateral loads were studied to understand their stress distribution [4–6], in-plane free vibration [7,8], and impact/rebound [3]. Plus, considering size effect, the free vibration of 2D nanorings under lateral loads was also investigated [9,10]. In particular, Chen et al. [11] studied a connected carbon nanoring, which was found to have a great Young's modulus, and then, based on this work, Feng and Liew [1] studied the critical buckling displacement and shape of the laterally tensioned basic

element—a single carbon nanoring. However, the studies on the mechanical behavior of the carbon nanoring were based on molecular mechanics or molecular dynamics.

To the best knowledge of the authors, 3D ring structures subjected to axial loads have been extensively studied due to their fascinating properties, such as buckling patterns and energy absorption of cylindrical shells [12–14], but their mechanical properties under lateral forces have rarely been studied. In this regard, a single tube was laterally compressed by Ghosh et al. [15], as an energy absorber, and the mechanical behavior of round nested metallic tubes systems (i.e., combined cylindrical tubes) between two rigid plates, has been studied [16,17], also as energy absorbers. The quasi-static lateral compression, post-collapse, and crushing behavior of the tube systems were experimentally and numerically analyzed and later reviewed by Olabi et al. [18].

The above literature focused on a ring subjected to a single lateral concentrated force or a pair of lateral forces along a diameter. Also, there are multi-pairs of concentrated forces centrally acting on a ring, which often exist in the form of a basic element in a complex structure, for example, circular joints subjected to two or three pairs of lateral forces in the centre-symmetric tetragonal or hexagonal honeycombs [19]. Thus, in view of rings subjected to few pairs of centrally acting forces along diameters [17,19], we here extend them to a general case, for which a single ring is subjected to multi-pairs of equal, radial, concentrated forces evenly distributed around the ring, and find the load-deformation or load-strain energy relationships.

2 Theoretical models

The elastica theory is always employed to characterize very large deformations of curved structures, where the shear and axial deformations are not considered, for example, it is used to study a micro-beam, droplet, carbon nanotube (CNT) ring adhered on a substrate [20], and interestingly, an island-bridge model in a stretchable electronic, in which the large deformation of the bridge structure was modeled as an elastica beam with both ends fixed [21]. However, it is noted that real curved structures are not elastica, and they usually deform plastically when subjected to large loads [2,3], plus, the shear and axial deformations cannot be neglected when the bar or plate forming the curved structures is thick; otherwise, the Timoshenko beam theory has to be employed, in this case, it reduces the bending rigidity of the curved structures due to the involvement of the shear effect, and improves the structural deformation. Here, the theory for thin structures is used to study the ring elastica under multi-pairs of equal forces acting along diameters, and in-plane/out-of-plane stability is not considered. To comprehensively describe the ring’s mechanical behaviors, the ring under both compress-

ion and tension are treated, and the compressive case comes first.

2.1 Multi-pairs of equal radial compressive forces

Here, we exemplify a 2D ring structure with three pairs of evenly distributed equal compressive forces as shown in Fig. 1a. From Fig. 1a, it is easily generalized that for the ring under N pairs of evenly distributed equal forces, only a $1/(2N)$ portion of the ring needs to be studied. Moreover, as the compressive forces increase, the ring experiences six states from 0 to V as marked in Fig. 1b. State 0 is an initial ring subjected to no force. The other five states can be divided into two groups. Group 1 (states I, II) has negative curvature and group 2 (states II–V) has both positive and negative curvatures. Apparently, state II which is common to both groups is critical. Then, basing on the group division and considering only radial displacements at points A and B , the half structures of the two groups are simplified as shown in Fig. 1c, d, and the forces analyzed are shown in Fig. 1e, f.

2.1.1 Group 1 (States I, II)

(1) State I (Red profile in Fig. 1b)

From Fig. 1e, under a vertical external force F at the end point A , the vertical force at the end point B equals F because of the equilibrium in the vertical direction. Moreover, due to the guided constraint, the resultant force (or constraint reaction) of the horizontal force F' and the vertical force F at the end point B must be tangential to deformed rings at the point, thus the horizontal force F' is calculated by $F' = F \cot \varphi$ with $\varphi = \pi/(2N)$. Applying moment equilibrium with respect to the end point A , we obtain

$$-M_A + M_B = Fb\xi(a, b), \text{ with} \\ \xi(a, b) = \frac{1 - (a/b) \cos \varphi}{\sin \varphi}, \tag{1}$$

where M_A and M_B are moments acting at the end points A and B , respectively; a and b are distances from the end points A and B to the origin O , i.e., ring center, respectively. Thus, employing the elastica theory, the moment-curvature relationship of an arbitrary point $P(x, y)$ is expressed as [22]

$$D \frac{d\theta}{ds} = - [M_B - F(b \sin \varphi - x) + F'(y - b \cos \varphi)], \tag{2}$$

where D is the bending rigidity of the ring, for bars $D = EI$ and for thin plates $D = Et^3/[12(1 - \nu^2)]$, (s, θ) is the curvilinear coordinate of the point P . Here, θ is defined to be positive when the tangent line of the point P pointing at the

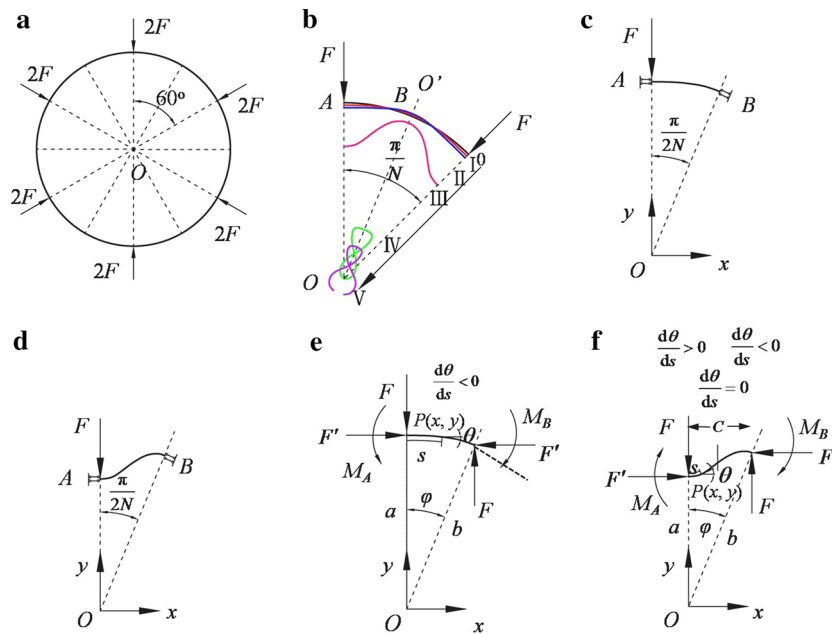


Fig. 1 (Color online) Schematics and force analysis of a ring with N -pairs of equal compressive radial forces. **a** A 2D ring with three pairs of equal compressive radial forces; **b** $1/(2N)$ ring with N -pairs of equal compressive forces, and six states with the increasing compressive forces; **c** half structure of the group 1; **d** half structure of the group 2; **e** force analysis of the group 1; **f** force analysis of the group 2

end point B is counterclockwise relative to the positive x axis, otherwise, it is negative, thus when the point P moves from A to B , θ monotonously varies from 0 to $-\varphi$. Deriving Eq. (2) with respect to the curvilinear coordinate s and considering the geometrical relationship $dx/ds = \cos \theta$ and $dy/ds = \sin \theta$, it is rewritten as

$$D \frac{d^2 \theta}{ds^2} = -F \cos \theta - F' \sin \theta, \tag{3}$$

multiplying both sides of Eq. (3) by $d\theta/ds$, and integrating it by substituting $F' = F \cot \varphi$, its solution is obtained as

$$\frac{1}{2} D \left(\frac{d\theta}{ds} \right)^2 = F \frac{\cos(\theta + \varphi)}{\sin \varphi} + C. \tag{4}$$

Boundary conditions provide $d\theta/ds|_{\theta=0} = -M_A/D$ and $d\theta/ds|_{\theta=-\varphi} = -M_B/D$, which lead to two expressions with respect to M_A and M_B . Invoking Eq. (1) and solving the two expressions, we obtain another equation:

$$M_A + M_B = \frac{2D}{b} \zeta(a, b), \text{ with } \zeta(a, b) = \frac{1 - \cos \varphi}{1 - (a/b) \cos \varphi}. \tag{5}$$

Then, combining Eqs. (1), (4), and (5), the unknowns M_A , M_B , and C are calculated as

$$\begin{aligned} M_A &= -\frac{Fb}{2} \xi(a, b) + \frac{D}{b} \zeta(a, b), \\ M_B &= \frac{Fb}{2} \xi(a, b) + \frac{D}{b} \zeta(a, b), \\ C &= \frac{M_A^2}{2D} - \frac{F \cos \varphi}{\sin \varphi}, \text{ or } \frac{M_B^2}{2D} - \frac{F}{\sin \varphi}. \end{aligned} \tag{6}$$

The length of the arc AB is $l = \varphi R$, and defining a set of non-dimensional quantities, $k^2 = Fl^2/D$, $\bar{a} = a/l$, $\bar{b} = b/l$, $\bar{s} = s/l$, the non-dimensional curvature is solved from Eq. (4) as

$$\begin{aligned} \frac{d\theta}{d\bar{s}} &= -\sqrt{\frac{2}{\sin \varphi}} k \sqrt{K^2 + \cos(\theta + \varphi)}, \text{ with} \\ K^2 &= \frac{\sin \varphi}{2k^2 \bar{b}^2} \left[\frac{k^2 \bar{b}^2}{2} \xi(\bar{a}, \bar{b}) - \zeta(\bar{a}, \bar{b}) \right]^2 - \cos \varphi, \end{aligned} \tag{7}$$

here, since θ monotonously decreases from 0 to $-\varphi$, $d\theta/d\bar{s}$ is negative, and the curvilinear coordinate of the arbitrary point P is integrated as

$$\bar{s}(\theta) = \sqrt{\sin \varphi} \frac{p}{k} \left[F\left(\frac{\varphi}{2}, p\right) - F\left(\frac{\varphi}{2} + \frac{\theta}{2}, p\right) \right], \tag{8}$$

where $p = \sqrt{2/(1 + K^2)}$, and $F(\psi, p) = \int_0^\psi 1/\sqrt{1 - p^2 \sin^2 \psi} d\psi$ is the incomplete elliptical integral of the first kind, in which ψ represents a general amplitude. Because axial and shear deformations are neglected, the inextensible condition $\bar{s}(-\varphi) = 1$ holds, and we arrive at the following equation

$$\sqrt{\sin \varphi} \frac{p}{k} F\left(\frac{\varphi}{2}, p\right) = 1. \tag{9}$$

To determine the deformation of the structures, the Cartesian coordinates of the point P are always calculated by integrating the differential vector $d\mathbf{r}(\theta) = d(\bar{x}, \bar{y})^T = (\cos \theta, \sin \theta)^T d\bar{s}$, where $\bar{x} = x/l$ and $\bar{y} = y/l$, i.e.,

$$\mathbf{r}(\theta) = -\frac{1}{k} \sqrt{\frac{\sin \varphi}{2}} \left[\int_0^\theta \frac{\cos \theta}{\sqrt{K^2 + \cos(\theta + \varphi)}} d\theta, \int_0^\theta \frac{\sin \theta}{\sqrt{K^2 + \cos(\theta + \varphi)}} d\theta \right]^T + (0, \bar{a})^T, \tag{10}$$

furthermore, Eq. (10) is solved as (See the derivation in ‘‘Appendix A’’):

$$\mathbf{r}(\theta) = -\frac{1}{k} \sqrt{\frac{\sin \varphi}{2}} \begin{bmatrix} \sin \varphi & \cos \varphi \\ \cos \varphi & -\sin \varphi \end{bmatrix} \begin{bmatrix} A(\theta) \\ B(\theta) \end{bmatrix} + \begin{pmatrix} 0 \\ \bar{a} \end{pmatrix}, \tag{11}$$

where

$$\begin{aligned} A(\theta) &= -2 \left[\sqrt{K^2 + \cos(\theta + \varphi)} - \sqrt{K^2 + \cos \varphi} \right], \\ B(\theta) &= -\sqrt{2} p \left\{ K^2 \left[F\left(\frac{\theta}{2} + \frac{\varphi}{2}, p\right) - F\left(\frac{\varphi}{2}, p\right) \right] \right. \\ &\quad \left. - \frac{2}{p^2} \left[E\left(\frac{\theta}{2} + \frac{\varphi}{2}, p\right) - E\left(\frac{\varphi}{2}, p\right) \right] \right\}, \end{aligned} \tag{12}$$

in which $E(\psi, p) = \int_0^\psi \sqrt{1 - p^2 \sin^2 \psi} d\psi$ is the incomplete elliptical integral of the second kind, ψ also represents a general amplitude. It is readily seen that Eqs. (11) and (12) give $\mathbf{r}(0) = (0, \bar{a})^T$, which is the coordinate of the end point A . For the end point B , Eq. (11) should satisfy $\mathbf{r}(-\varphi) = \bar{b}(\sin \varphi, \cos \varphi)^T$, which are expressed as

$$\begin{aligned} \bar{x}(-\varphi) &= -\frac{1}{k} \sqrt{\frac{\sin \varphi}{2}} [A(-\varphi) \sin \varphi + B(-\varphi) \cos \varphi] \\ &= \bar{b} \sin \varphi, \\ \bar{y}(-\varphi) &= -\frac{1}{k} \sqrt{\frac{\sin \varphi}{2}} [A(-\varphi) \cos \varphi - B(-\varphi) \sin \varphi] + \bar{a} \\ &= \bar{b} \cos \varphi. \end{aligned} \tag{13}$$

Addressing Eq. (13), on the one hand, we multiply the first equation by $\sin \varphi$, the second by $\cos \varphi$, and sum them together; on the other hand, we multiply the first equation by $\cos \varphi$, the second by $\sin \varphi$, and subtract the first by the second, then we obtain

$$\begin{aligned} -\frac{1}{k} \sqrt{\frac{\sin \varphi}{2}} A(-\varphi) &= \bar{b} - \bar{a} \cos \varphi, \\ -\frac{1}{k} \sqrt{\frac{\sin \varphi}{2}} B(-\varphi) &= \bar{a} \sin \varphi. \end{aligned} \tag{14}$$

It is noted that the first expression in Eq. (14) holds (See the proof in ‘‘Appendix B’’). Replacing θ in $B(\theta)$ of Eq. (12) by $-\varphi$ and using the inextensible condition Eq. (9), the second expression of Eq. (14) is re-expressed as

$$\bar{a} \sin \varphi + K^2 - \frac{2\sqrt{\sin \varphi}}{kp} E\left(\frac{\varphi}{2}, p\right) = 0. \tag{15}$$

According to Eqs. (9) and (15), the shape parameters \bar{a} and \bar{b} reflecting the deformation of the ring, are implicit functions of the force k , which determines the profile of the ring.

Moreover, the elastic strain energy is derived as

$$U_1 = \int_0^l \frac{1}{2} D \left(\left| \frac{d\theta}{ds} \right| - \kappa_0 \right)^2 ds, \tag{16}$$

where $\kappa_0 = 1/R = \varphi/l$ is the initial curvature (i.e., curvature of the state 0). Re-expressing it in a non-dimensional form and employing Eq. (7), we find:

$$\begin{aligned} \bar{U}_1 &= \frac{U_1 l}{D} = \frac{1}{2} \int_0^1 \left(\left| \frac{d\theta}{d\bar{s}} \right| - \kappa_0 l \right)^2 d\bar{s} \\ &= \frac{2}{\sqrt{\sin \varphi}} \frac{k}{p} E\left(\frac{\varphi}{2}, p\right) - \frac{\varphi^2}{2}. \end{aligned} \tag{17}$$

(2) State II (Blue profile in Fig. 1b)

The critical state II transiting from states I and III in Fig. 1b is a particular case common to both states. In this state, the curvature at the end point A starts changing from negative to positive (Fig. 1e, f), i.e., $d\theta/d\bar{s}|_{\theta=0} = 0$. Employing Eq. (7), the zero curvature provides $K^2 = -\cos \varphi$, which further leads to $p = \csc(\varphi/2)$ by $p = \sqrt{2/(1 + K^2)}$. Then, substituting $p = \csc(\varphi/2)$ into the inextensible condition (9), the critical force $k_{cr,1}$ is expressed as

$$k_{cr,1} = \sqrt{2 \cot\left(\frac{\varphi}{2}\right)} F\left(\frac{\varphi}{2}, \csc\left(\frac{\varphi}{2}\right)\right), \tag{18}$$

and inserting $K^2 = -\cos \varphi$, $p = \csc(\varphi/2)$ and $k_{cr,1}$ into Eq. (15), the shape parameter $\bar{a}_{cr,1}$ is calculated as

$$\bar{a}_{cr,1} = \csc \varphi \left[\cos \varphi + (1 - \cos \varphi) \frac{E\left(\frac{\varphi}{2}, \csc\left(\frac{\varphi}{2}\right)\right)}{F\left(\frac{\varphi}{2}, \csc\left(\frac{\varphi}{2}\right)\right)} \right], \tag{19}$$

moreover, $K^2 = -\cos \varphi$ also leads to the following expression by the definition of K^2 in Eq. (7)

$$k^2 \bar{b}^2 = 2 \frac{\zeta(\bar{a}, \bar{b})}{\xi(\bar{a}, \bar{b})}, \tag{20}$$

and inserting $k_{cr,1}$ and $\bar{a}_{cr,1}$ into Eq. (20), $\bar{b}_{cr,1}$ is calculated as

$$\bar{b}_{cr,1} = \cot \varphi \cos \varphi + (1 - \cos \varphi) \frac{1 + \cot \varphi \cdot E\left(\frac{\varphi}{2}, \csc \frac{\varphi}{2}\right)}{F\left(\frac{\varphi}{2}, \csc \frac{\varphi}{2}\right)}. \tag{21}$$

2.1.2 Group 2 (States II, III, IV, and V)

State II is the critical state between groups 1 and 2, and it has already been dealt within Sect. 2.1.1.(2), thus we do not intend to derive it in this section.

(3) State III (Plum profile in Fig. 1b)

As stated before, differently from state I, the positive and negative curvatures exist simultaneously as the force increases, and there is an inflection point C , see Fig. 1f. For the AC part, $d\theta/d\bar{s} > 0$, and for the CB part, $d\theta/d\bar{s} < 0$, thus at the inflection point C , $d\theta/d\bar{s}|_{\theta_{cr}} = 0$, where θ_{cr} is the angular coordinate of the point C . Here we mark the two parts AC and CB by subscripts 1 and 2, respectively, and the curvilinear coordinates of the point P in the two parts are calculated by integrating the following curvature expressions

$$\begin{aligned} \frac{d\theta}{d\bar{s}_1} &= \sqrt{\frac{2}{\sin \varphi}} k \sqrt{K^2 + \cos(\theta + \varphi)}, \theta \in (0, \theta_{cr}), \\ \frac{d\theta}{d\bar{s}_2} &= -\sqrt{\frac{2}{\sin \varphi}} k \sqrt{K^2 + \cos(\theta + \varphi)}, \theta \in (\theta_{cr}, -\varphi), \end{aligned} \tag{22}$$

where K^2 is the same as that in Eq. (7), and Eq. (22) is integrated as

$$\begin{aligned} \bar{s}_1(\theta) &= \sqrt{\sin \varphi} \frac{p}{k} \left[F\left(\frac{\varphi}{2} + \frac{\theta}{2}, p\right) - F\left(\frac{\varphi}{2}, p\right) \right], \\ &\theta \in (0, \theta_{cr}), \\ \bar{s}_2(\theta) &= \sqrt{\sin \varphi} \frac{p}{k} \left[F\left(\frac{\varphi}{2} + \frac{\theta_{cr}}{2}, p\right) - F\left(\frac{\varphi}{2} + \frac{\theta}{2}, p\right) \right], \\ &\theta \in (\theta_{cr}, -\varphi). \end{aligned} \tag{23}$$

Then, the inextensible condition provides $\bar{s}_1(\theta_{cr}) + \bar{s}_2(-\varphi) = 1$, which is further expressed as

$$\sqrt{\sin \varphi} \frac{p}{k} \left[2F\left(\frac{\varphi}{2} + \frac{\theta_{cr}}{2}, p\right) - F\left(\frac{\varphi}{2}, p\right) \right] = 1. \tag{24}$$

Similar to Eqs. (10)–(12), the Cartesian coordinate of the point P in the part AC is computed as

$$\mathbf{r}_1(\theta) = \frac{1}{k} \sqrt{\frac{\sin \varphi}{2}} \begin{bmatrix} \sin \varphi \cos \varphi \\ \cos \varphi - \sin \varphi \end{bmatrix} \begin{bmatrix} A_1(\theta) \\ B_1(\theta) \end{bmatrix} + \begin{pmatrix} 0 \\ \bar{a} \end{pmatrix}, \tag{25}$$

where $A_1(\theta)$ and $B_1(\theta)$ are same as Eq. (12), but the upper limit of the angular coordinate θ is replaced by θ_{cr} instead of $-\varphi$. Equation (25) also provides the coordinates of the end point A , i.e., $\mathbf{r}_1(0) = (0, \bar{a})^T$. For the part CB , the Cartesian coordinate is calculated as

$$\mathbf{r}_2(\theta) = -\frac{1}{k} \sqrt{\frac{\sin \varphi}{2}} \begin{bmatrix} \sin \varphi \cos \varphi \\ \cos \varphi - \sin \varphi \end{bmatrix} \begin{bmatrix} A_2(\theta) \\ B_2(\theta) \end{bmatrix} + \mathbf{r}_1(\theta_{cr}), \tag{26}$$

where

$$\begin{aligned} A_2(\theta) &= -2\sqrt{K^2 + \cos(\theta + \varphi)}, \\ B_2(\theta) &= -\sqrt{2}p \left\{ K^2 \left[F\left(\frac{\theta}{2} + \frac{\varphi}{2}, p\right) - F\left(\frac{\theta_{cr}}{2} + \frac{\varphi}{2}, p\right) \right] \right. \\ &\quad \left. - \frac{2}{p^2} \left[E\left(\frac{\theta}{2} + \frac{\varphi}{2}, p\right) - E\left(\frac{\theta_{cr}}{2} + \frac{\varphi}{2}, p\right) \right] \right\}. \end{aligned} \tag{27}$$

As stated above, at the inflection point C , $d\theta/d\bar{s}|_{\theta_{cr}} = 0$ holds, which leads to $K^2 + \cos(\theta_{cr} + \varphi) = 0$ from Eq. (22) and $A_2(\theta_{cr}) = B_2(\theta_{cr}) = 0$ from Eq. (27), thus, Eq. (26) provides $\mathbf{r}_2(\theta_{cr}) = \mathbf{r}_1(\theta_{cr})$, which ensures the continuity of the parts AC and CB at the point C . Moreover, using Eq. (26) and considering $\mathbf{r}_2(-\varphi) = \bar{b}(\sin \varphi, \cos \varphi)^T$, then like with the treatment of Eq. (13), we obtain

$$\begin{aligned} \frac{1}{k} \sqrt{\frac{\sin \varphi}{2}} [A_1(\theta_{cr}) - A_2(-\varphi)] + \bar{a} \cos \varphi &= \bar{b}, \\ \frac{1}{k} \sqrt{\frac{\sin \varphi}{2}} [B_1(\theta_{cr}) - B_2(-\varphi)] - \bar{a} \cos \varphi &= 0. \end{aligned} \tag{28}$$

As in the proof in ‘‘Appendix B’’, the first equation in Eq. (28) always holds, and the second expression yields

$$\begin{aligned} \bar{a} \sin \varphi + K^2 \\ - \frac{2\sqrt{\sin \varphi}}{kp} \left[2E\left(\frac{\varphi}{2} + \frac{\theta_{cr}}{2}, p\right) - E\left(\frac{\varphi}{2}, p\right) \right] &= 0, \end{aligned} \tag{29}$$

employing Eqs. (24) and (29), the shape parameters \bar{a} and \bar{b} can be solved by a given force k .

For state III, the elastic strain energy is calculated in a non-dimensional form as

$$\begin{aligned} \bar{U}_{III} &= \frac{U_{III}l}{D} = \frac{1}{2} \int_0^1 \left(\left| \frac{d\theta}{d\bar{s}} \right| - \kappa_0 l \right)^2 d\bar{s} = \frac{2}{\sqrt{\sin \varphi}} \frac{k}{p} \\ &\times \left[2E\left(\frac{\theta_{cr} + \varphi}{2}, p\right) - E\left(\frac{\varphi}{2}, p\right) \right] - 2\varphi\theta_{cr} - \frac{\varphi^2}{2}. \end{aligned} \tag{30}$$

(4) State IV (Green profile in Fig. 1b)

State IV, in Fig. 1b, is the second critical state being between states III and V. In this case, $\bar{a}_{cr,2} = 0$. Employing the inextensible condition Eqs. (24) and (29), the force $k_{cr,2}$ and shape parameter $\bar{b}_{cr,2}$ can be obtained.

(5) State V (Purple profile in Fig. 1b)

The calculation of state V is same as state III, so we will not repeat the process here.

From analyzing states I to V, we can conclude that when the force k varies from 0 to $k_{cr,1}$, state I exists when k varies from $k_{cr,1}$ to $k_{cr,2}$, state III exists and state V emerges when k is beyond $k_{cr,2}$.

2.2 Multi-pairs of equal tensile forces

Section 2.1 deals with the five compressive states of the ring. For the tensile case, its curvature is similar to that of state I in the compressive case, i.e., $d\theta/d\bar{s} < 0$, where θ changes from 0 to $-\varphi$, and what we need do is to replace the force F in Eqs. (4) and (6) with $-F$. Then, the curvature of the arbitrary point P is expressed as

$$\frac{d\theta}{d\bar{s}} = -\sqrt{\frac{2}{\sin\varphi}} k \sqrt{K^2 - \cos(\theta + \varphi)}, \text{ with}$$

$$K^2 = \frac{\sin\varphi}{2k^2\bar{b}^2} \left[\frac{k^2\bar{b}^2}{2} \xi(\bar{a}, \bar{b}) + \zeta(\bar{a}, \bar{b}) \right]^2 + \cos\varphi, \quad (31)$$

and the curvilinear coordination is solved as

$$\bar{s}(\theta) = \sqrt{\sin\varphi} \frac{p}{k} \times \left[F\left(\frac{\pi + \varphi}{2}, p\right) - F\left(\frac{\pi + \varphi}{2} + \frac{\theta}{2}, p\right) \right]$$

$$\text{with } K^2 = \frac{\sin\varphi}{2k^2\bar{b}^2} \left[\frac{k^2\bar{b}^2}{2} \xi(\bar{a}, \bar{b}) + \zeta(\bar{a}, \bar{b}) \right]^2 + \cos\varphi, \quad (32)$$

where $p = \sqrt{2/(1 + K^2)}$. Invoking the inextensible condition $\bar{s}(-\varphi) = 1$, we find

$$\sqrt{\sin\varphi} \frac{p}{k} \left[F\left(\frac{\pi + \varphi}{2}, p\right) - F\left(\frac{\pi}{2}, p\right) \right] = 1. \quad (33)$$

Similar to the Cartesian expressions Eqs. (11) and (25) of the point P , its vector is calculated as

$$\mathbf{r}(\theta) = -\frac{1}{k} \sqrt{\frac{\sin\varphi}{2}} \begin{bmatrix} \sin\varphi & \cos\varphi \\ \cos\varphi & -\sin\varphi \end{bmatrix} \begin{bmatrix} A(\theta) \\ B(\theta) \end{bmatrix} + \begin{pmatrix} 0 \\ \bar{a} \end{pmatrix}, \quad (34)$$

where

$$A(\theta) = 2 \left[\sqrt{K^2 - \cos(\theta + \varphi)} - \sqrt{K^2 - \cos\varphi} \right],$$

$$B(\theta) = \sqrt{2} p \left\{ K^2 \left[F\left(\frac{\theta}{2} + \frac{\pi + \varphi}{2}, p\right) - F\left(\frac{\pi + \varphi}{2}, p\right) \right] - \frac{2}{p^2} \left[E\left(\frac{\theta}{2} + \frac{\pi + \varphi}{2}, p\right) - E\left(\frac{\pi + \varphi}{2}, p\right) \right] \right\}, \quad (35)$$

considering the coordinates of the end point $B\mathbf{r}(-\varphi) = \bar{b}(\sin\varphi, \cos\varphi)^T$ and substituting it into Eq. (34), like the treatment of Eq. (13), we obtained the following expression

$$-\frac{1}{k} \sqrt{\frac{\sin\varphi}{2}} A(-\varphi) = \bar{b} - \bar{a} \cos\varphi,$$

$$-\frac{1}{k} \sqrt{\frac{\sin\varphi}{2}} B(-\varphi) = \bar{a} \sin\varphi. \quad (36)$$

Similarly, the first equation in Eq. (37) also always holds, and the second expression yields

$$\bar{a} \sin\varphi - K^2 + \frac{2\sqrt{\sin\varphi}}{kp} \left[E\left(\frac{\pi + \varphi}{2}, p\right) - E\left(\frac{\pi}{2}, p\right) \right] = 0. \quad (37)$$

Combing Eqs. (33) and (37), the shape parameters \bar{a} and \bar{b} can be solved by a given k .

Moreover, the non-dimensional elastic strain energy of the tensile case is calculated as

$$\bar{U}_T = \frac{U_T l}{D} = \frac{1}{2} \int_0^1 \left(\left| \frac{d\theta}{d\bar{s}} \right| - \kappa_0 l \right)^2 d\bar{s} = \frac{2}{\sqrt{\sin\varphi}} \frac{k}{p} \times \left[E\left(\frac{\pi + \varphi}{2}, p\right) - E\left(\frac{\pi}{2}, p\right) \right] - \frac{\varphi^2}{2}. \quad (38)$$

3 Results and discussion

Here, we consider four loading cases, i.e., $N = 1, 2, 3, 4$. For each case, one tensile state and six compressive states are theoretically treated, and the specific non-dimensional forces k for the seven states are set to be $-6, 0, 0.8k_{cr,1}, k_{cr,1}, 0.8k_{cr,2}, k_{cr,2}, 2k_{cr,2}$. Correspondingly, the commercial software ABAQUS/Standard was used to verify the theoretical results. The radius of the ring in the FE geometrical model is 10 mm, and the cross-section of the ring bar is circular, with the radius set to 0.1 mm. The linear-elastic constitutive behavior of the ring material is used and its Young's modulus and Poisson's ratio are 210 GPa and 0.25, respectively. Thanks to symmetry, the FE model was simplified by studying a $1/(2N)$ ring, see Fig. 2. The model contains 100 2-node B21 elements, which include the shear effect, and 101 uniformly distributed nodes. The loading process is displacement controlled. Since the analysis is a quasi-static

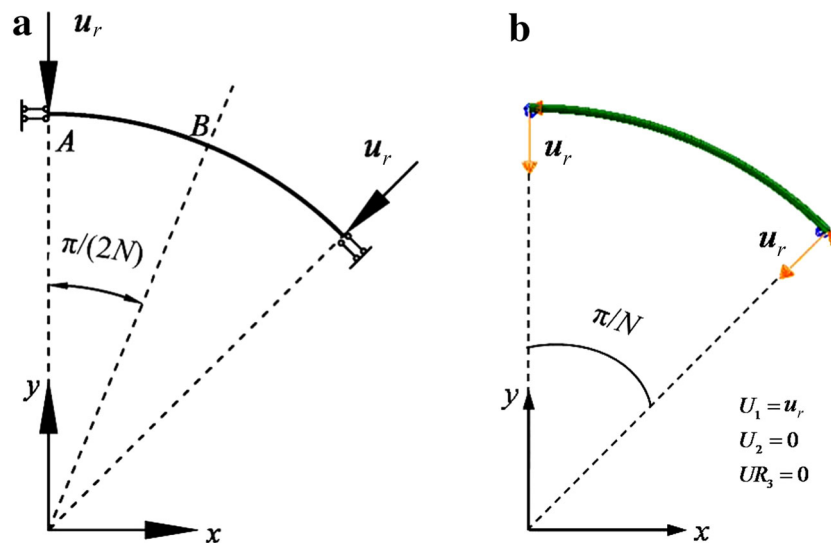


Fig. 2 (Color online) **a** Diagram and **b** mesh and boundary condition of the finite element model. U_1 and U_2 are the displacements in the radial and circumferential directions, respectively, and UR_3 is the rotation

large deformation, an automatic incrementing type is used to ensure the convergence. As for the continuous deformation process of the whole ring, it can be seen in *supplementary video materials*.

3.1 Deformation profiles

Each of the seven specific states, is denoted by an orange, black, red, blue, plum, green, and purple profile, respectively, see Fig. 3. The results show that the theoretical prediction and FE simulation agree very well (solid lines for theoretical results and the discrete markers for FE results in Fig. 3). It is easily seen that in the tensile state, the ring tends to be a regular polygon with $2N$ sides as the force increases, for example, when $N = 2, 3, 4$, the ring approaches square, regular hexagon, and regular octagon (orange profiles in Fig. 3b–d), respectively. In the compressive states, the critical state II (blue profiles in Fig. 3a–d) gradually approaches the initial ring (black profiles in Fig. 3a–d) as N increases, in particular, the critical state II in the case of $N = 4$ almost coincides with the initial profile. That is to say, as N increases, the scope of state I (red profiles in Fig. 3a–d) between state 0 and the critical state II becomes narrower and narrower; instead, state III (plum profiles in Fig. 3a–d) between the state II and the critical state IV (green profiles in Fig. 3a–d), gets wider and wider. Moreover, if the force exceeds the first critical value, i.e., $0.8k_{cr,2}$, $k_{cr,2}$, the ring deforms into flower-like patterns, and when the force increases beyond the second critical value, i.e., $2k_{cr,2}$, the ring reversely tends to be a regular polygon, but with $2N$ knots (purple profiles in Fig. 3a–d). In particular, when $N = 1$, the ring deformed by $0.8k_{cr,2}$ (plum profiles in Fig. 3a) is

similar to the dog-bone shaped single-wall carbon nanotube bundles, and when $N = 3$, the ring deformed by -6 (orange line in Fig. 3c) resembles the hexagonal single-wall carbon nanotube bundles [23,24]. In this regard, due to their similar cross-sectional shapes, the elastic strain energy of carbon nanotubes could be solved by the present method. However, for nanomaterials, we have to say that the theory based on the elastica theory is continuous, and care should be exercised when dealing with discrete nanomaterials, e.g., nanotubes. In addition, when structural size enters the nano-scale, surface effects have to be taken into account [25].

As stated at the beginning of Sect. 2, the static deformation theory of a 2D elastica ring derived mathematically does not include the in-plane/out-of-plane stability. Here, in the FE model, the in-plane/out-of-plane stability is guaranteed to use the displacement loading mode [26] and the 2D beam element. It is noted that the displacement loading mode of the FE model is different from the present theory, which is based on the force loading mode. In reality, the two loading modes may result in different structural stabilities under the compressive loads, because the ring structures are always stable in the displacement loading manner due to the prescribed displacement, and often unstable in the force loading manner due to the critical buckling force. Moreover, it is not easy to arrive at the deformations of states I–V as the structural instability of the 2D ring structures is present during the compressive process. In particular, the states I–III are also valid for 3D ring structures, which, due to their larger axial dimensions, are more stable during the deformation process than the 2D ring. The out-of-plane instability of the 2D rings is mainly caused by

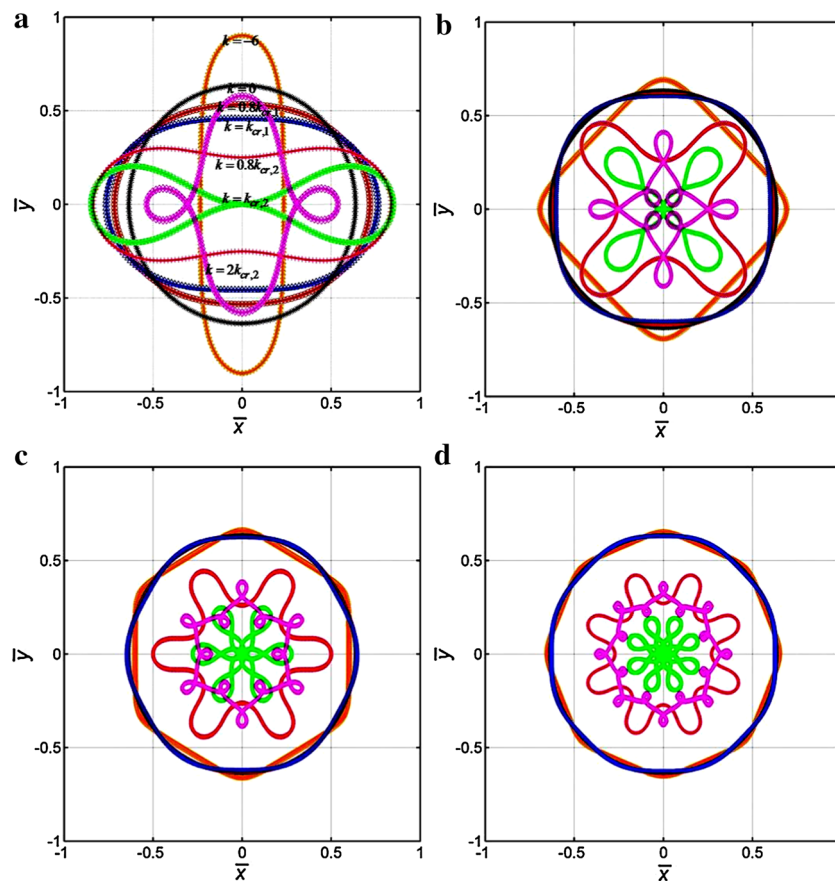


Fig. 3 (Color online) Comparison between theoretical and finite element results under N -pairs of equal forces for each state. **a** $N = 1$; **b** $N = 2$; **c** $N = 3$; **d** $N = 4$. Note, the solid profiles are theoretical results, and the discrete marker profiles are FE results, because of the tightness between state 0, state I, and state II, it is not easy to distinguish them in **c, d**

two aspects. One is the out-of-plane deformation of the ring arch in Fig. 1b under lateral loads [27] before self-contact, which may occur in states I–III. The other is the out-of-plane kinematics after self-contact [28], which may occur in states III–V; furthermore, a knot will be formed as the force increases, and this physical phenomenon can be often found in the study of other thin elastic rods [28, 29]. Thus, states IV and V, only occur when the ring is self-intersected or out-of-plane kinematics are permitted, and the characterization of self-intersection and out-of-plane kinematics that are both physically reasonable and mathematically precise, is very difficult [29].

To illustrate the effectiveness of the present theory, topological experiments were carried out to compare the geometrical similarity using a Nitrile Butadiene Rubber (NBR) ring, whose characteristics allowed it to be controlled more easily when entering into unstable states. The NBR ring was constrained between a base and transparent cover to control its out-of-plane kinematics. The corresponding loading cases were performed by tensioning cotton threads previously glued to the relevant points on the ring. For the tensile

case, the tension was applied outwards, but for the compressive case, the tension was applied inwards. It is worth mentioning that in spite of using NBR for the ring, it was still very difficult to create the state V due to the complexity of the pattern and the instability in the ring. In any case, the experimental result was obtained by integrating the raw pictures in “Appendix C” of ESM and reported in Fig. 4, which partially show the consistence of the present theory.

3.2 Shape parameters and elastic strain energy

For the loading case with N pairs of forces, the force F , the shape parameters a and b , energy U are non-dimensionalized by $l = \varphi R = \frac{\pi}{2N} R = \frac{L}{4N}$, where $L = 2\pi R$ is the perimeter of the ring, and they are expressed as $k = \frac{L}{4N} \sqrt{\frac{F}{D}}$, $\bar{a} = \frac{4Na}{L}$, $\bar{b} = \frac{4Nb}{L}$, and $\bar{U} = \frac{U}{D} \cdot \frac{L}{4N}$, respectively. Thus, because of the variable N from 1 to 4, the comparison of the shape parameters and elastic strain energy needs to be unified, and $Nk = \frac{L}{4} \sqrt{\frac{F}{D}}$, $\frac{\bar{a}}{N} = \frac{4a}{L}$, $\frac{\bar{b}}{N} = \frac{4b}{L}$, and $N\bar{U}$ are compared here.

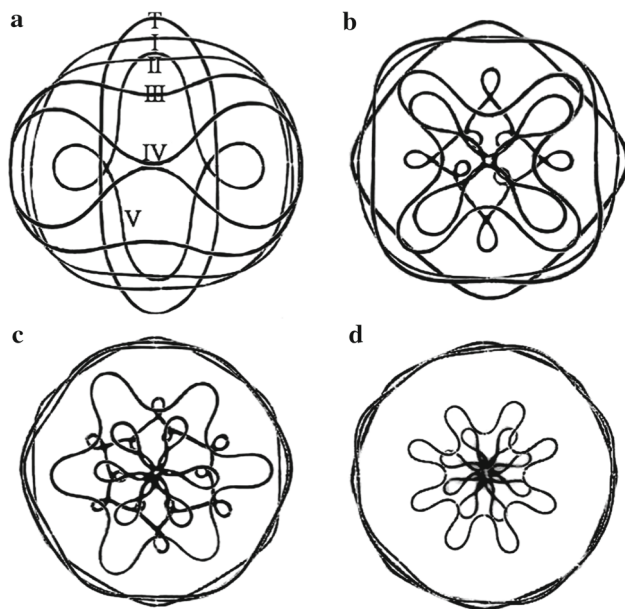


Fig. 4 Topological experiments of extrinsic similar shapes as their counterparts in Fig. 3

Then, for the four above loading cases, the relationships of the shape parameters and elastic strain energies with forces are plotted in Fig. 5.

From Fig. 5a, it can be seen that the theoretical results (thin lines) match the finite element results (thick lines) very well. Regarding the scopes of the parameters \bar{a} (solid lines in Fig. 5a) and \bar{b} (dashed lines in Fig. 5a), we consider two extreme states, one is tensile and the other is compressive, and as stated before, the profiles of the ring in the two extreme states are approximate regular polygons, then through geometrical analysis of the polygons, the shape parameter a varies from $-l \csc \varphi$ to $l \csc \varphi$, and b from $-l \cot \varphi$ to $l \cot \varphi$. Thus, normalized by the arc length of l , the non-dimensional shape parameters \bar{a} and \bar{b} vary in the intervals of $(-\csc \varphi, \csc \varphi)$ and $(-\cot \varphi, \cot \varphi)$, respectively. In the tensile case, the non-dimensional force k is negative. As the force increases, the shape parameters \bar{a} and \bar{b} increase and decrease, respectively, moreover, \bar{a}/N tends to $\csc \varphi/N$, and \bar{b}/N tends to $\cot \varphi/N$. For example, if there is one pair of equal tensile forces (blue lines in Fig. 5a), i.e., $N = 1$ and $\varphi = \frac{\pi}{2}$, \bar{a} tends to be 1.0, and \bar{b} to be 0. This means that the y -coordinate of point A approaches a quarter of the ring's perimeter, and point B tends to the center of the ring. Plus, as N increases, \bar{a} and \bar{b} tend to $\frac{2}{\pi}$. In the compressive case, the force k is positive. As the force increases, \bar{a} always decreases, but \bar{b} increases first and then decreases, which can be clearly observed in Fig. 3a, i.e., in the case of $N = 1$, \bar{b} increases from state 0 (black profile) to state IV (green profile), and then decrease afterward (purple profile), similarly, \bar{a}/N tends to $-\csc \varphi/N$, and \bar{b}/N tend to $-\cot \varphi/N$. Meanwhile, as N

increases, the maximum of \bar{b} and its corresponding \bar{a} both tend to $\frac{2}{\pi}$ (see Fig. 5a and its inset), and its corresponding forces also increase (see the inset in Fig. 5a). This indicates that when N tends to infinity, the ring's shape is still a circle even though a great compressive force is applied, and this can be used to explain a well-known phenomenon: when an egg is held in one hand, it does not break even when a large handgrip force is applied.

Figure 5b depicts the elastic strain energy stored in the $1/(2N)$ ring as the force increases. Even though the results from the two methods do not match very well as the profiles in Fig. 3 and shape parameters in Fig. 5a, they are still comparable. This is because the bending strain energy is only considered in the theory (thin lines), and compared to the bending deformation, the tensile and shear strain energies are neglected thanks to their smallness. However, the data from the finite element analysis (thick lines) includes all three, and thus the finite element result is a little greater than the theoretical results, and the difference grows as the external force increases. Plus, it shows that in the tensile case, the elastic strain energy is very small, and as N increases, the elastic strain energy decreases. This is due to the inextensible condition which determines smaller and smaller deformation as N increases. The compressive case has a very different behaviour to the tensile case, namely, as N increases, the elastic strain energy increases, and this is due to a large number of applied forces on the ring with a greater deformation of the ring.

The present theoretical model for a ring structure is very useful for analyzing the mechanical behavior of micro- and nano-devices in microelectromechanical systems (MEMs), nanoelectromechanical systems (NEMS), and electronics [30]; however, in these cases, distinct physical mechanisms, such as surface effect and size effect, in micro- or nano-scale should be further considered. In particular, for the stretchability and flexibility of electronics, the mechanical safety and electronic performance under large strain is not guaranteed [21], thus the strain distribution of the micro-structure, particularly, the maximum strain is of much importance. It is critical to predict accurately the maximum strain using a theoretical model so that premature failure of the structure can be avoided by an optimal design. For the present ring structure, the well-known strain of the bending Euler beam along a cross-section is expressed as: $\varepsilon(y) = y \frac{d\theta}{ds} = \frac{M}{EI} y$, where y is the distance from a material point to the neutral axis of the cross-section, thus with a uniform cross-section, the maximum strain depends on the curvature/moments and the cross-section size. From Eq. (6), we can see that in the compressive case, $M_B > M_A$ always holds, and in the tensile case, $M_B < M_A$, so it is very easy to find the location of maximum strain, and further avoid the failure of the structure.

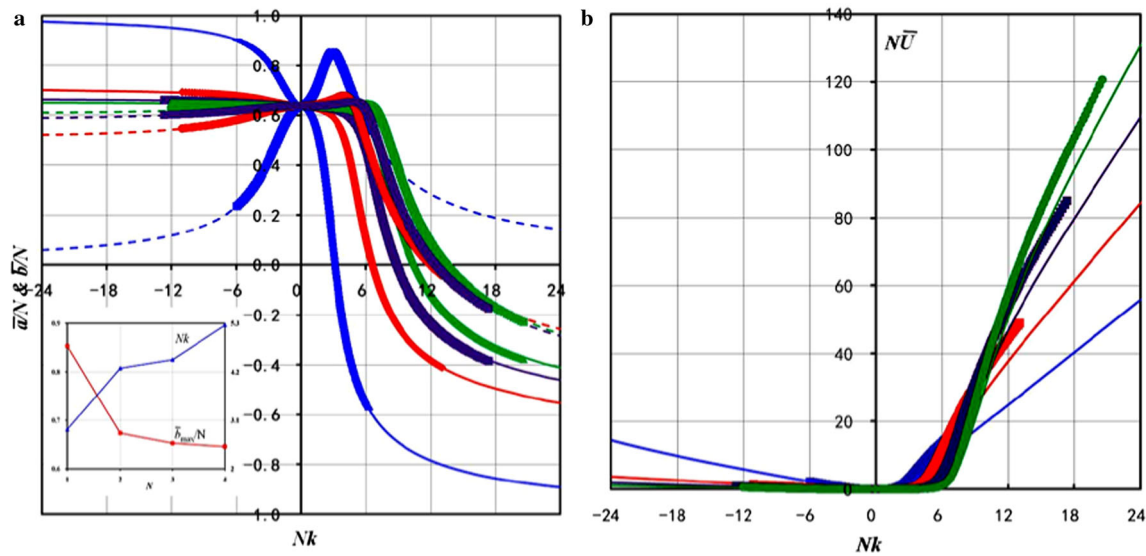


Fig. 5 (Color online) Shape parameters of loaded rings and strain energy stored in the $1/(2N)$ rings. **a** Variations of the shape parameters \bar{a} and \bar{b} , for the theoretical results, the solid lines represent the shape parameter \bar{a} , and the dashed denote \bar{b} ; **b** strain energy stored in $1/(2N)$ ring. Noted that the blue, red, purple, and green lines represent $N = 1, 2, 3, 4$ in order

Finally, it is worth mentioning that care should be exercised when using this method for rings under unevenly distributed forces, which will induce non-symmetric configurations, and this is because the positions of the equivalent guided points A and B are not apparent as with the present work, and they must be determined through calculation.

4 Conclusions

In summary, we have developed a set of theories for a ring subjected to multi-pairs of evenly distributed equal radial forces. The theory reflects the relationship between the pair number of forces, the value of the forces, the shape, and the strain energy. In the tensile case, there is only one state, while in the compressive case, the ring experiences six states. The results show very good agreement between the theory and finite element results. Interestingly, no matter whether the ring is compressed or tensioned by N -pairs of equal forces, it always tends to form a regular polygon with $2N$ sides as the force increases, and with a compressive force the ring deforms into flower-like patterns. These results could be helpful in studying the mechanics of ring structures under lateral concentrated loads, such as the micro- or nano-devices in the MEM or NEM systems.

Acknowledgements This work is partially supported by the National Natural Science Foundation of China (Grants 31300780, 11272091, 11422222, and 31470043), the Fundamental Research Funds for the Central Universities (Grant 2242016R30014), and ARC (Grant FT140101152). N.M.P. is supported by the European Research Council PoC 2015 “Silkene” (Grant 693670), by the European Commission H2020 under the Graphene Flagship Core 1 (Grant 696656) (WP14

“Polymer Nanocomposites”), and under the FET Proactive “Neurofibres” (Grant 732344).

Appendix A

The coordinate vector (10) of the point P can be solved as

$$\begin{aligned}
 \mathbf{r}(\theta) &= -\frac{1}{k} \sqrt{\frac{\sin \varphi}{2}} \left[\int_0^\theta \frac{\cos \theta}{\sqrt{K^2 + \cos(\theta + \varphi)}} d\theta, \right. \\
 &\quad \left. \int_0^\theta \frac{\sin \theta}{\sqrt{K^2 + \cos(\theta + \varphi)}} d\theta \right]^T + (0, \bar{a}]^T \\
 &= -\frac{1}{k} \sqrt{\frac{\sin \varphi}{2}} \left[\int_0^\theta \frac{\cos(\theta + \varphi - \varphi)}{\sqrt{K^2 + \cos(\theta + \varphi)}} d\theta, \right. \\
 &\quad \left. \int_0^\theta \frac{\sin(\theta + \varphi - \varphi)}{\sqrt{K^2 + \cos(\theta + \varphi)}} d\theta \right]^T + (0, \bar{a}]^T \\
 &= -\frac{1}{k} \sqrt{\frac{\sin \varphi}{2}} \left\{ \left[\sin \varphi \int_0^\theta \frac{\sin(\theta + \varphi)}{\sqrt{K^2 + \cos(\theta + \varphi)}} d\theta \right. \right. \\
 &\quad \left. \left. + \cos \varphi \int_0^\theta \frac{\cos(\theta + \varphi)}{\sqrt{K^2 + \cos(\theta + \varphi)}} d\theta \right], \right. \\
 &\quad \left. \left[\cos \varphi \int_0^\theta \frac{\sin(\theta + \varphi)}{\sqrt{K^2 + \cos(\theta + \varphi)}} d\theta \right. \right.
 \end{aligned}$$

$$\begin{aligned}
 & \left. - \sin \varphi \int_0^\theta \frac{\cos(\theta + \varphi)}{\sqrt{K^2 + \cos(\theta + \varphi)}} d\theta \right\}^T + (0, \bar{a})^T \\
 &= -\frac{1}{k} \sqrt{\frac{\sin \varphi}{2}} \begin{bmatrix} \sin \varphi & \cos \varphi \\ \cos \varphi & -\sin \varphi \end{bmatrix} \\
 & \times \left[\int_0^\theta \frac{\sin(\theta + \varphi)}{\sqrt{K^2 + \cos(\theta + \varphi)}} d\theta, \right. \\
 & \left. \int_0^\theta \frac{\cos(\theta + \varphi)}{\sqrt{K^2 + \cos(\theta + \varphi)}} d\theta \right]^T + (0, \bar{a})^T \\
 &= -\frac{1}{k} \sqrt{\frac{\sin \varphi}{2}} \begin{bmatrix} \sin \varphi & \cos \varphi \\ \cos \varphi & -\sin \varphi \end{bmatrix} \begin{bmatrix} A(\theta) \\ B(\theta) \end{bmatrix} + \begin{pmatrix} 0 \\ \bar{a} \end{pmatrix}, \tag{A1}
 \end{aligned}$$

where

$$\begin{aligned}
 A(\theta) &= \int_0^\theta \frac{\sin(\theta + \varphi)}{\sqrt{K^2 + \cos(\theta + \varphi)}} d\theta \\
 &= -2 \left[\sqrt{K^2 + \cos(\theta + \varphi)} - \sqrt{K^2 + \cos \varphi} \right], \\
 B(\theta) &= \int_0^\theta \frac{\cos(\theta + \varphi)}{\sqrt{K^2 + \cos(\theta + \varphi)}} d\theta \\
 &= -\sqrt{2} p \left\{ K^2 \left[F\left(\frac{\theta}{2} + \frac{\varphi}{2}, p\right) - F\left(\frac{\varphi}{2}, p\right) \right] \right. \\
 & \quad \left. - \frac{2}{p^2} \left[E\left(\frac{\theta}{2} + \frac{\varphi}{2}, p\right) - E\left(\frac{\varphi}{2}, p\right) \right] \right\}. \tag{A2}
 \end{aligned}$$

Appendix B

Replacing θ in $A(\theta)$ of Eq. (12) by $-\varphi$ and inserting $A(-\varphi)$ into the first expression of Eq. (14), we obtain

$$\begin{aligned}
 & -\frac{1}{k} \sqrt{\frac{\sin \varphi}{2}} \left[-2 \left(\sqrt{K^2 + 1} - \sqrt{K^2 + \cos \varphi} \right) \right] \\
 &= \bar{b} - \bar{a} \cos \varphi. \tag{B1}
 \end{aligned}$$

Re-arranging Eq. (B1), the following expression arrives

$$\sqrt{K^2 + 1} - \sqrt{\frac{\sin \varphi}{2}} k \bar{b} \xi(\bar{a}, \bar{b}) = \sqrt{K^2 + \cos \varphi}. \tag{B2}$$

Squaring both sides of the Eq. (B2), it is re-expressed as

$$\begin{aligned}
 & 1 - \cos \varphi - 2\sqrt{K^2 + 1} \sqrt{\frac{\sin \varphi}{2}} k \bar{b} \xi(\bar{a}, \bar{b}) \\
 & + \frac{\sin \varphi}{2} k^2 \bar{b}^2 \xi^2(\bar{a}, \bar{b}) = 0. \tag{B3}
 \end{aligned}$$

Considering the expression of K^2 in Eq. (7), we find

$$\begin{aligned}
 K^2 + 1 &= \frac{\sin \varphi}{2k^2 \bar{b}^2} \left[\frac{k^2 \bar{b}^2}{2} \xi(\bar{a}, \bar{b}) - \zeta(\bar{a}, \bar{b}) \right]^2 + 1 - \cos \varphi \\
 &= \frac{\sin \varphi}{2k^2 \bar{b}^2} \left\{ \left[\frac{k^2 \bar{b}^2}{2} \xi(\bar{a}, \bar{b}) - \zeta(\bar{a}, \bar{b}) \right]^2 \right. \\
 & \quad \left. + 2k^2 \bar{b}^2 \frac{1 - \cos \varphi}{\sin \varphi} \right\} \\
 &= \frac{\sin \varphi}{2k^2 \bar{b}^2} \left\{ \left[\frac{k^2 \bar{b}^2}{2} \xi(\bar{a}, \bar{b}) - \zeta(\bar{a}, \bar{b}) \right]^2 \right. \\
 & \quad \left. + 2k^2 \bar{b}^2 \xi(\bar{a}, \bar{b}) \zeta(\bar{a}, \bar{b}) \right\} \\
 &= \frac{\sin \varphi}{2k^2 \bar{b}^2} \left[\frac{k^2 \bar{b}^2}{2} \xi(\bar{a}, \bar{b}) + \zeta(\bar{a}, \bar{b}) \right]^2. \tag{B4}
 \end{aligned}$$

Substituting Eq. (B4) into Eq. (B3), the left side of Eq. (B3) is expressed as

$$\begin{aligned}
 & 1 - \cos \varphi - 2\sqrt{\frac{\sin \varphi}{2}} \frac{1}{k \bar{b}} \left[\frac{k^2 \bar{b}^2}{2} \xi(\bar{a}, \bar{b}) + \zeta(\bar{a}, \bar{b}) \right] \\
 & \times \sqrt{\frac{\sin \varphi}{2}} k \bar{b} \xi(\bar{a}, \bar{b}) + \frac{\sin \varphi}{2} k^2 \bar{b}^2 \xi^2(\bar{a}, \bar{b}) \\
 &= 1 - \cos \varphi - \sin \varphi \left[\frac{k^2 \bar{b}^2}{2} \xi^2(\bar{a}, \bar{b}) + \xi(\bar{a}, \bar{b}) \zeta(\bar{a}, \bar{b}) \right] \\
 & \quad + \frac{\sin \varphi}{2} k^2 \bar{b}^2 \xi^2(\bar{a}, \bar{b}) \\
 &= 1 - \cos \varphi - \sin \varphi \xi(\bar{a}, \bar{b}) \zeta(\bar{a}, \bar{b}) \\
 &= 1 - \cos \varphi - (1 - \cos \varphi) \\
 &= 0. \tag{B5}
 \end{aligned}$$

Thus, the derivation of Eqs. (B1) – (B5) proves that the first expression in Eq. (14) always holds.

References

1. Feng, C., Liew, K.W.: A molecular mechanics analysis of the buckling behavior of carbon nanorings under tension. *Carbon* **47**, 3508–3514 (2009)
2. Karamanos, S.A., Eleftheriadis, C.: Collapse of pressurized elastoplastic tubular members under lateral loads. *Int. J. Mech. Sci.* **46**, 35–56 (2004)
3. Bao, R.H., Yu, T.X.: Impact and rebound of an elastic-plastic ring on a rigid target. *Int. J. Mech. Sci.* **91**, 55–63 (2015)
4. Timoshenko, S.: On the distribution of stress in a circular ring compressed by two forces along a diameter. *Phil. Mag.* **44**, 1014–1019 (1922)
5. Chianese, R.B., Erdlac, R.J.: The general solution to the distribution of stresses in a circular ring compressed by two forces acting along a diameter. *Q. J. Mech. Appl. Math.* **41**, 239–247 (1988)

6. Batista, M., Usenik, J.: Stresses in a circular ring under two forces acting along a diameter. *J. Strain Anal. Eng.* **31**, 75–78 (1996)
7. Rao, S.S., Sundararajan, V.: In-plane flexural vibrations of circular rings. *J. Appl. Mech.* **36**, 620–625 (1969)
8. Kirkhope, J.: In-plane vibration of a thick circular ring. *J. Sound Vib.* **50**, 219–227 (1977)
9. Wang, C.M., Duan, W.H.: Free vibration of nanorings/arches based on nonlocal elasticity. *J. Appl. Phys.* **104**, 014303 (2008)
10. Moosavi, H., Mohammadi, M., Farajpour, A., et al.: Vibration analysis of nanorings using nonlocal continuum mechanics and shear deformable ring theory. *Phys. E* **44**, 135–140 (2011)
11. Chen, N., Lusk, M.T., van Duin, A.C.T., et al.: Mechanical properties of connected carbon nanorings via molecular dynamics simulation. *Phys. Rev. B* **72**, 085416 (2005)
12. von Karman, T.: The buckling of thin cylindrical shells under axial compression. *J. Aeronaut. Sci.* **8**, 303–312 (1941)
13. Bardi, F.C., Yun, H.D., Kyriakides, S.: On the axisymmetric progressive crushing of circular tubes under axial compression. *Int. J. Solids Struct.* **40**, 3137–3155 (2003)
14. Marsolek, J., Reimerdes, H.G.: Energy absorption of metallic cylindrical shells with induced non-axisymmetric folding patterns. *Int. J. Impact Eng.* **30**, 1209–1223 (2004)
15. Ghosh, S.K., Johnson, W., Reid, S.R., et al.: On thin rings and short tubes subjected to centrally opposed concentrated loads. *Int. J. Mech. Sci.* **23**, 183–194 (1981)
16. Reddy, T., Reid, S.: Phenomena associated with the lateral crushing of metal tubes between rigid plates. *Int. J. Solids Struct.* **16**, 545–562 (1980)
17. Gupta, N., Sekhon, G., Gupta, P.: Study of lateral compression of round metallic tubes. *Thin Wall Struct.* **43**, 895–922 (2005)
18. Olabi, A.G., Morris, E., Hashmi, M.S.J.: Metallic tube type energy absorbers: a synopsis. *Thin Wall Struct.* **45**, 706–726 (2007)
19. Miller, W., Smith, C.W., Scarpa, F., et al.: Flatwise buckling optimization of hexachiral and tetrachiral honeycombs. *Compos. Sci. Technol.* **70**, 1049–1056 (2010)
20. Liu, J.L., Xia, R.: A unified analysis of a micro-beam, droplet and CNT ring adhered on a substrate: calculation of variation with movable boundaries. *Acta Mech. Sin.* **29**, 62–72 (2013)
21. Li, R., Li, M., Su, Y., et al.: An analytical mechanics model for the island-bridge structure of stretchable electronics. *Soft Matter* **9**, 8476–8482 (2013)
22. Bisshopp, K.E., Drucker, D.C.: Large deflection of cantilever beams. *Q. Appl. Math.* **3**, 272–275 (1945)
23. Elliott, J.A., Sandler, J.K., Windle, A.H., et al.: Collapse of single-wall carbon nanotubes is diameter dependent. *Phys. Rev. Lett.* **92**, 095501 (2004)
24. Pugno, N.: The design of self-collapsed super-strong nanotube bundles. *J. Mech. Phys. Solids* **58**, 1397–1410 (2010)
25. Chen, Q., Pugno, N.: Competition between in-plane buckling and bending collapses in nanohoneycombs. *Europhys. Lett.* **98**, 16005 (2012)
26. Bažant, Z.P., Cedolin, L.: *Stability of Structures: Elastic, Inelastic, Fracture and Damage Theories*. World Scientific, Singapore, 278–294 (2010)
27. Guo, Y.L., Zhao, S.Y., Pi, Y.L., et al.: An experimental study on out-of-plane inelastic buckling strength of fixed steel arches. *Eng. Struct.* **98**, 118–127 (2015)
28. Batista, M.: A simplified method to investigate the stability of cantilever rod equilibrium forms. *Mech. Res. Commun.* **67**, 13–17 (2015)
29. Gonzalez, O., Maddocks, J.H., Schuricht, F., et al.: Global curvature and self-contact of nonlinearly elastic curves and rods. *Calc. Var.* **14**, 29–68 (2002)
30. Ma, Y., Jang, K.I., Wang, L., et al.: Design of strain-limiting substrate materials for stretchable and flexible electronics. *Adv. Funct. Mater.* **26**, 5345–5351 (2016)

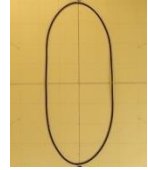
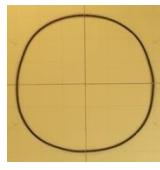
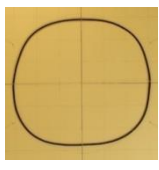
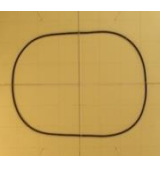
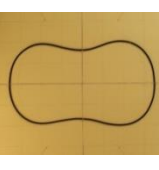
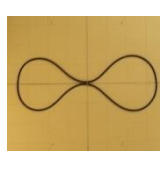
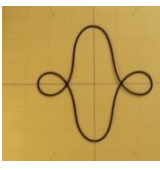
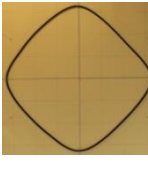
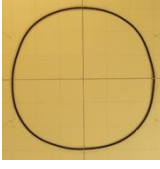
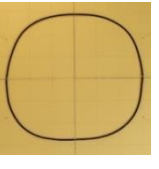
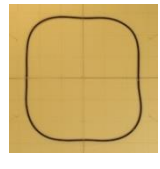
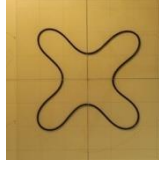

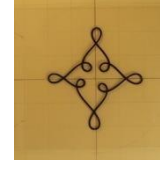
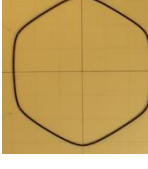
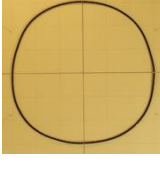
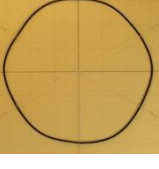
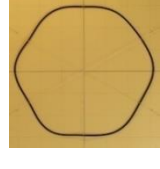



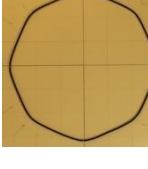
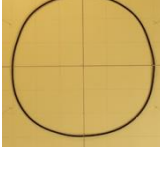
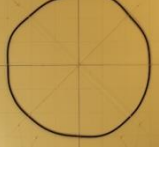
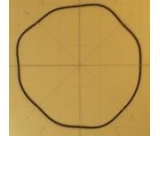
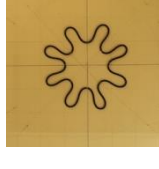

Tensile case	Compressive case					
	State 0	State I	State II	State III	State IV	State V
						
						
						
						

Figure S1. The patterns formed by the ring whilst being acted on by pairs of forces as described in the theoretical part of this paper. From top to bottom the pairs of forces on the ring were $N=1, 2, 3$ & 4 . Noted that the state V of the case $N = 4$ is not available thanks to the complexity, and state 0 is not shown in Fig. 4.